Quintero-Jaime, AF.; Hafed-Khatiri, S.; Huerta, F.; Quijada, C.; Montilla, F. (2022). Dynamics and coherence of photoexcited states in polyfluorene films with ordered chain phases. Journal of Materials Chemistry C. 10(32):11801-11809. https://doi.org/10.1039/d2tc02770d

Dynamics and Coherence of Photoexcited States in Polyfluorene Films with Ordered Chain Phases

Andrés Felipe Quintero-Jaime[a], Salma Hafed-Khatiri[a], Francisco Huerta[b], César Quijada[b], Francisco Montilla*[,a]

[a] Departamento de Química Física and Instituto Universitario de Materiales de Alicante (IUMA), Universidad de Alicante, Carretera San Vicente s/n, 03690, Alicante, Spain

[b] Departamento de Ingenieria Textil y Papelera, Universitat Politecnica de Valencia, Plaza Ferrandiz y Carbonell, 1, E-03801, Alcoy, Spain

*Corresponding author: francisco.montilla@ua.es

Abstract

Understanding the optical and electronic excitations in conjugated polymers, their delocalization, and dynamics is of paramount importance for improving the performance of optoelectronic devices. The structure of the conjugated polymer in solid state, the presence of ordered domains, and conformational subunits strongly affect exciton and polaron interactions. The effect of the crystalline structure of polyfluorene films on exciton dynamics was studied by a combination of electrochemical and spectroscopic methods. Optoelectronic alterations caused by the *p*-doping process strongly suggest that the electrochemical charge injection occurs mainly in the more ordered β-phase. Evidence for the presence of either α- or β-phases is supported by the different behavior of the fluorescence quenching at increasing doping levels (the quenching elements appear more homogeneously distributed in the α-PFO phase). Estimated singlet exciton coherence lengths indicate that it delocalizes over 20 repeat units in the α-PFO phase, but it extends only over 14 units for β-PFO.

Keywords: Electrofluorochromism, Exciton diffusion, β-phase structure, Huang-Rhys factor, Exciton coherence

1. Introduction

The development of optoelectronic devices based on conjugated polymers has undergone an enormous evolution since the early 90s. This family of materials has shown a tremendous technological impact with applications ranging from light-emitting diodes, photovoltaic cells, and thin-film transistors [1,2] to new innovative technologies, such as flexible or wearable OLED devices [3], emission lasers [4], and light-based healthcare systems [5]. The combination of their outstanding electronic properties, characteristic of π-conjugated organic semiconductors, with other physical features, such as transparency or low density, and the versatility of the fabrication process has provided significant advantages over alternative materials [6].

However, electronic properties responsible for charge transport and exciton dynamics are very sensitive to the conjugated polymer's molecular nature and structural conformation [7]. Therefore, understanding and optimizing charge mobility, jointly with exciton generation and losses [8], are challenging aspects to enhance the semiconductor *in operando* conditions and, consequently, the performance of practical photoelectronic devices. Photoexcited states in conjugated polymers were usually described as Frenkel excitons due to the low dielectric constant [9,10]. However, after photoexcitation, Frenkel-like hole-electron pairs suffer vibrational relaxation that drives to charge delocalization along the polymer chain, exhibiting a mixed behavior [11,12]. Moreover, excitons can show a dual character in conjugated polymers showing π-stacking, behaving as Wannier-Mott type excitons along a polymer chain, with the hole-electron separation ranging over several repeat units, whereas excitons are of the Frenkel type across chains, where charge separation is restricted to closest neighboring chains [13].

The concept of coherence length, as derived from the wave-like nature of the excited states, is a key aspect of the interpretation of exciton dynamics. Due to the inherent

disorder of the polymers, this coherent range is limited to small portions of the chain (usually less than 10 monomer units) with Forster-like hopping between segments driving to incoherent diffusive hopping [14]. In general terms, large coherence lengths are preferred since they lead to more efficient optoelectronic devices [15,16].

Among the variety of optically active organic materials, polyfluorenes have been extensively investigated and employed as efficient building blocks for electronic devices. These polymers are widely employed as blue emitters in polymer-based LEDs due to their high photoluminescence quantum yield and chemical stability [17,18]. Specifically, poly-(9,9)-dioctylfluorene (PFO) is widely used in such applications thanks to the ability to form ordered phases with tunable optical properties. Depending on the PFO manufacturing process (i.e. solvent, temperature, method of synthesis) and the application of subsequent treatments such as annealing [18], a polymorphic behavior in the conformation of the PFO chain is observed in the solid-state. In this way, a combination of amorphous or glassy domains (α-phase) and more crystalline parts (β-phase) can be obtained by changes in the intermonomer torsion angle of the PFO backbone [19,20]. A higher twist angle in the β-conformation endows the PFO chains with a coplanar structure, with a higher conjugation length and, consequently, a more effective charge transport [21]. In contrast, conformational changes of polymer chains at the glassy α-phase provide localized excitations along the backbone. Differences in the conformational structure of PFO films have implications on photoluminescence properties and carrier mobility [22–24], which significantly affect exciton generation and dynamics [18,25].

Shaw et al. [26] analyzed the singlet–singlet annihilation process of excitons in PFO samples at different relative content of β-phase. The quenching rate constant was found to depend on the crystallinity level, with a measured value up to 2.3 times higher than that obtained for a fully amorphous phase. Such a behavior agrees with the shorter exciton

lifetime values reported by Yu et al. [27] at PFO thin films with β-phase. Remarkably, interchain interactions in the β-conformation are due to the high stacking tendency of PFO chains, which results in lower energy emission and increased anisotropy of the photoluminescent emission [28].

Recently we reported a novel method to characterize exciton dynamics in light-emitting conjugated polymers [29]. The method makes it possible to quantify the exciton diffusion coefficient in conjugated polymers through quenching of their photoluminescent emission during electrochemical doping. Modeling the quenching process with Stern-Volmer kinetics enables a fast and reliable determination of exciton diffusion coefficients or exciton-polaron critical distances in conjugated polymers.

The present work explores the effect of polymer crystalline conformation on exciton dynamics. The use of spectroelectrochemistry is expected to reveal the role played by the conformational phasing of PFO on both polaron generation and exciton mobility. In addition, the quantitative analysis of spectroelectrochemical data should help, on the one hand, to determine exciton diffusion coefficients in polymer layers with different crystalline structures and, on the other, to estimate exciton coherence lengths. The relationship of this parameter with the microstructure of the polymer facilitates the optimization of optoelectronic devices based on these organic molecules.

2. Experimental Section

PFO was purchased from American Dye Source-ADS (average M_n 25000-150000, density 0.6243 g cm^{-3}, as determined by helium micro-ultrapycnometry, Quantachrome Instruments). Indium Tin Oxide (ITO)-coated glass substrates (Solems ITO-SOL 30, 25-35 Ω), were employed as the electrode support in all the *in situ* spectroelectrochemical experiments. Anhydrous acetonitrile (ACN, ≥99.8%), chloroform (≥99.9%), toluene

(≥99.9%), tetrabutylammonium hexafluorophosphate (TBA, ≥99%), and ferrocene (Fc, ≥97%) were supplied by Sigma-Aldrich.

Two distinct deposition procedures were followed to obtain PFO thin films with a high concentration of either α- or β-phase. PFO solution in chloroform (1 mg mL^{-1}) was drop-casted (20 µL) onto a pre-heated (120 ºC) ITO electrode to yield PFO films with a glassy structure (α-phase). Semicrystalline, β-phase-enriched, PFO films were obtained by drop-casting (20 µL) PFO in toluene solution (1 mg mL^{-1}) onto the ITO surface and let dry overnight at 4ºC. In the latter case, both the PFO solution and the ITO electrode were cooled previously at 4ºC. Electrodes were tagged as α-PFO (for pure glassy polymer films) and β-PFO for those films enriched in the crystalline phase.

Electrochemical measurements on PFO films were carried out in an EDAQ EA163 Potentiostat connected to a function generator (EG&G Parc model 175). The spectroelectrochemical cell was a conventional 1-cm optical path quartz fluorescence cuvette and was filled with a deaerated electrolyte. A platinum wire was used as the counter electrode and a silver wire as the reference electrode. Both electrodes were protected by glass capillary tubes immersed in the working electrolyte [30]. The reference electrode was calibrated against the ferricenium/ferrocene redox couple (Fc/Fc^{+}). Nitrogen gas flow was maintained over the working solution during all the experiments.

In situ photoluminescence (PL) and UV-vis spectra were acquired using a PTI QuantaMaster spectrofluorometer (model QM-62003SE) and an Ocean Optics spectrophotometer (Flame model Avantes DH-2000-S and optical fibers Ocean Optics QP100-2-UV/VIS GF052107-101), respectively. All the experiments were carried out at 10ºC to prevent ACN evaporation in an electrochemical cell with the three-electrode configuration described above. Other experimental details have been reported elsewhere [29].

3. Results and Discussion

The absorption and photoluminescence spectra of α- and β-PFO samples deposited on ITO substrates are represented in Fig. 1. The UV spectrum of the amorphous material (dashed line in Fig. 1A) shows a broad band centered at 390 nm. The corresponding PL spectrum (solid line) is characterized by three overlapped emission peaks at 425, 450, and 480 nm, associated with 0-0, 0-1, and 0-2 vibronic features of glassy PFO.

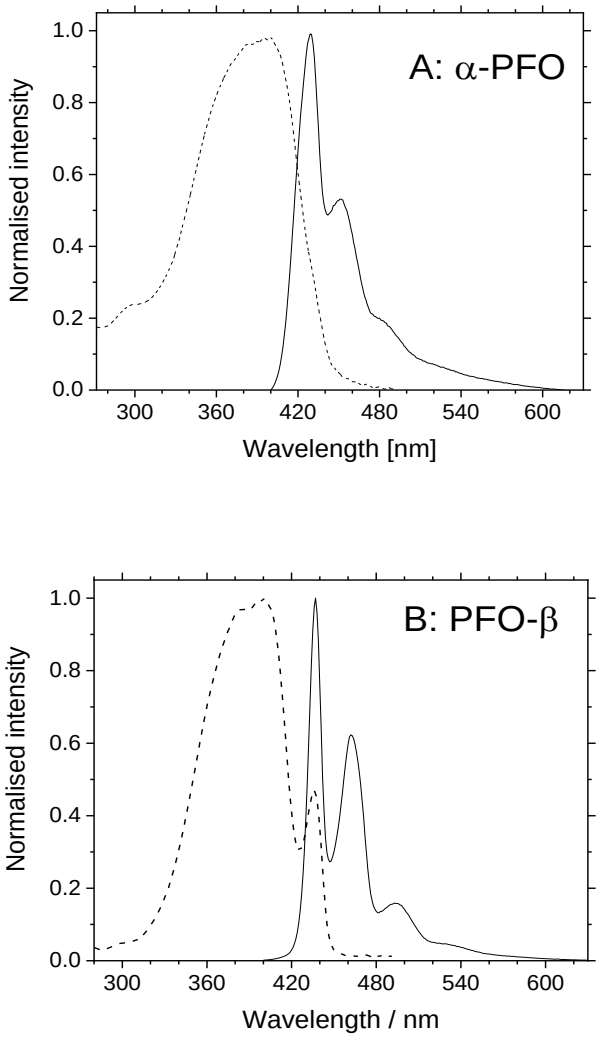

Figure 1. Absorption (dashed line) and emission (solid line) spectra (λ_{exc}= 380 nm) for PFO films deposited on quartz; **A)** glassy PFO and **B)** semicrystalline PFO.

The absorbance and emission spectra corresponding to a semicrystalline β-PFO thin film are shown in Fig. 1B. Here, the characteristic shoulder at around 432 nm corresponds to the 0-0 vibronic peak of the $S_0 \rightarrow S_1$ transition of the β-phase absorption. The red-shift of this absorption feature strongly suggests the presence of an extended π-conjugated structure in this material [25]. The PL spectrum displays a maximum at 437 nm and well-defined features at 462 and 494 nm corresponding to the vibronic progression of the PFO emission. It is known that the ordered, coplanar structure of the β-phase enables larger conjugation lengths in the polymer backbone. Reinforced interchain interactions promote π-π stacking on the one hand and materialization of localized low energy regions on the other [31,32]. Those low-energy sites are responsible for the red-shifting of absorptions and emissions from the β-phase [33]. From the relative areas of the corresponding absorption spectra, the amount of β-phase in the semicrystalline material was estimated at 33.5 ± 0.9 % [34,35].

3.1. Characterization of the electrochemical doping

The electrochemical *p*-doping of both PFO sample films was carried out by cyclic voltammetry in acetonitrile medium (see supporting information, Fig. S1). The onset potential (E_{onset}) for the oxidation of the semicrystalline sample (β-PFO) is shifted 140 mV to less positive potential compared to the pure α-PFO film. This means that the electrochemical generation of polaron species is energetically favored in the presence of crystalline, coplanar structures. This observation is in agreement with the results reported by Cadby *et al.* [25] based on photoinduced absorption spectroscopy. They found that the polaron yield in PFO samples with high β-phase content was around 10-15 times that obtained for α-PFO. The HOMO energy level of the polymer can be obtained from the stabilized cyclic voltammogram [36]. The values calculated from the CVs in Fig. S1 for glassy (–6.00 eV) and semicrystalline (–5.84 eV) PFO materials are very close to those

reported previously for other polyfluorene polymers [37]. Such figures reveal a connection between the HOMO level and the inner structure of PFO. It is worth mentioning that Kilina *et al*. [38] reached a similar conclusion by reporting that the presence of torsional angles and other defects in the backbone of amorphous polyfluorenes strongly affects the occupancy of electron levels, i.e. the HOMO/LUMO charge distribution.

The charge density (*CD*) injected into the PFO backbone at each point can be determined from the analysis of the stabilized cyclic voltammogram. In Figure 2, *CD* values are plotted against the bias potential, η, which is defined as the potential applied above the onset of the doping process ($\eta = E_{applied} - E_{onset}$). During the early stages of the oxidation process (up to a bias potential of about 0.15 V), α-PFO films need to be more polarized than β-PFO to reach the same doping level. This result is consistent with the existence of low-energy ordered segments with enhanced carrier mobility in β-PFO. However, above 0.15 V the injection of charge into the semicrystalline sample requires higher energy than that for the homogenous phase polymer. The origin of this unexpected behavior will be discussed in the following sections.

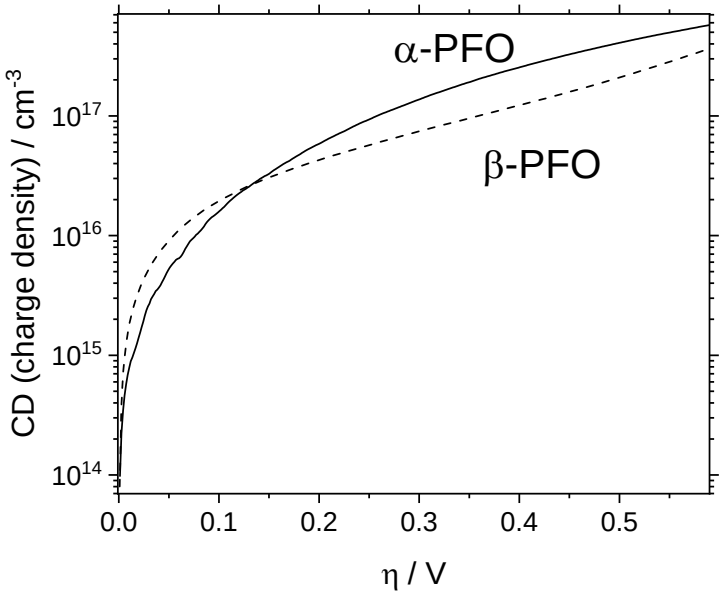

Figure 2. Injected charge density (*CD*) against bias potential (η) for the *p*-doping processes of glassy (α-PFO, solid line) and semicrystalline (β-PFO, dashed line) samples.

3.2. Spectroelectrochemical characterization

Optoelectronic alterations caused by *p*-doping in PFO films can be evaluated using electrochemically-induced UV-vis spectroscopy, a simple technique that consists of monitoring absorbance changes as the bias potential is increased. Figs. 3 shows differential UV-vis spectra recorded for glassy and semicrystalline PFO samples, respectively. Remarkably, the differential spectra of glassy PFO (Fig. 3A) do not show any electrochemically-induced absorption band at a low or moderate bias potential ($\eta<0.34$V). A negative (downward) band, corresponding to the bleaching of π-π* transitions, starts to develop above 0.34 V. This band intensifies as the positive charge injection leads to the formation of new intergap transitions. The absorption peak shifts from 410 to 405 nm at a higher doping level due to the oxidation of PFO chains, which causes progressively shorter conjugation lengths [39].

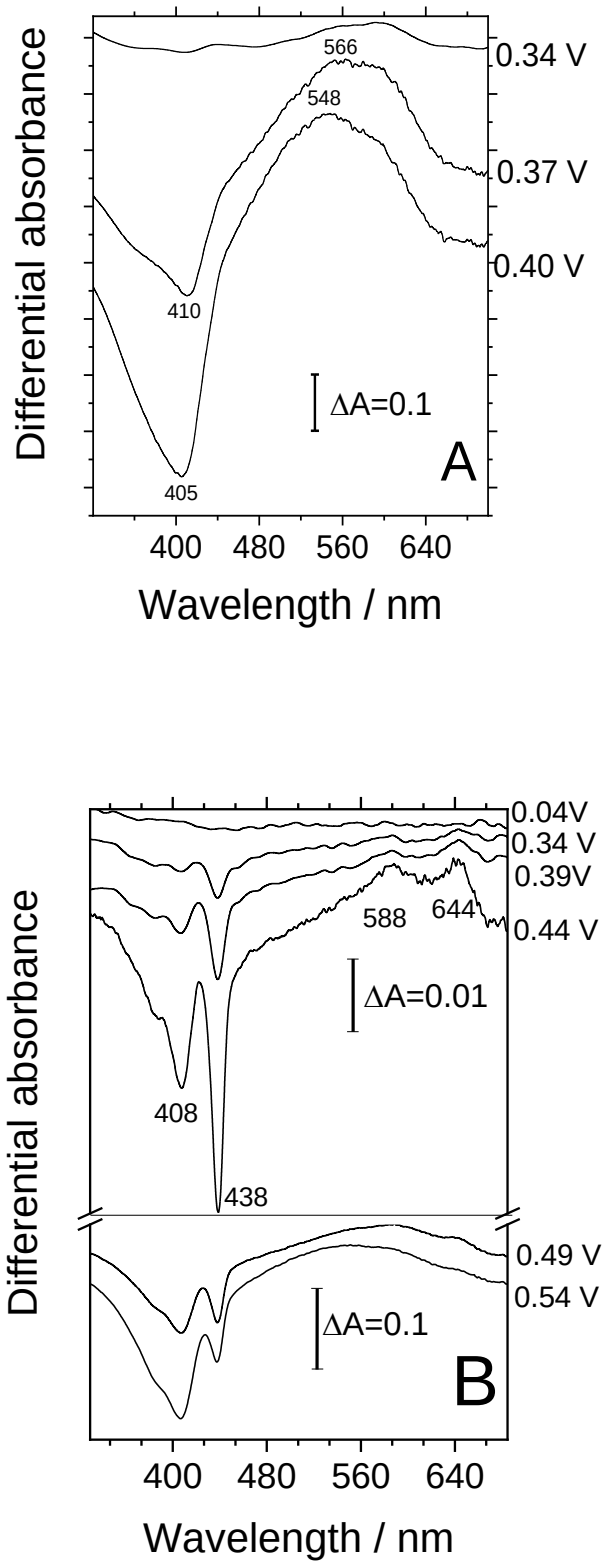

Figure 3. Electrochemically-induced UV-vis spectra collected during the p-doping process of A) a glassy α-PFO film and B) a semicrystalline β-PFO film

Coupled with the bleaching, a broad positive band peaking at 566 nm develops in the spectrum. This absorption is assigned to the electronic intragap transition of the polaron formed upon oxidation [40,41]. Further polarization produces intensification and progressive shifts towards shorter wavelengths. Similar hypsochromic drifts were attributed in the literature to the occurrence of compressed polarons in the PFO structure [34].

The differential UV-vis spectra corresponding to the semicrystalline β-PFO (Fig. 3B shows no clear electronic transitions below η=0.3 V. At higher bias, negative bands associated with the bleaching of PFO in β-phase progress at around 438 nm and 408 nm. These features correspond to 0-0 and 0-1 vibronic transitions, respectively (the Huang–Rhys factor calculated from the intensity ratio of the bleaching peaks is S= 0.6). The bleaching process of the β-phase occurs at a lower potential than that of the α-phase, which suggests that the rise of polaron species takes place preferentially in the more ordered β-phase, where a lower energy gap is found [42], in concordance with the lower E_{onset} value measured by cyclic voltammetry (Fig. S1). Positive bands appearing at 644 and 588 nm are therefore attributed to the absorption by charge carriers (polarons) residing in the β-phase.

The intensity of negative bands increases at higher bias potential, but no frequency shift is observed with the increasing doping level, in contrast to the bleaching of glassy domains. Furthermore, their intensity ratio remains unchanged up to a bias potential close to 0.44 V, thus suggesting again that charge is injected mostly into the β-phase.

At a bias potential higher than 0.44 V, the intensity of the negative peak at 408 nm grows significantly faster than that of the peak at 438 nm. The band at 408 shows

overlapping contributions from glassy phase 0-0 and β-phase 0-1 vibronic bands. The former signature starts dominating the spectra when charge injection is high enough to saturate chromophores in the crystalline segments.

Indeed, upward bands corresponding to polaron transitions intensify as the injected charge causes the saturation of chromophores. At that oxidation level, polaron species begin to be incorporated into the glassy domains of PFO.

A better knowledge of the role played by the crystalline morphology on the excited state properties can be gained from the analysis of changes in the fluorescence spectra of both PFO materials (Fig. 4). The *in situ* PL spectra recorded for α-PFO and β-PFO films at different doping levels are shown in Fig. 4A-B. In contrast with the *in situ* UV spectra, the polarization of the polymer beyond its semiconducting state produces modifications in light emission from very low doping levels. It is worth noting that the quenching of fluorescence in Fig. 4 starts at bias potentials significantly lower than those required to trigger the electronic absorptions of polaron species detected by UV (0.34 and 0.30 V for glassy and semicrystalline PFO, respectively). More specifically, about 40% of the initial fluorescence is quenched in α-PFO (η= 0.34 V, *CD*= 1.8×10^{17} cm^{-3}, Fig. 4C), while the emission loss amounts to 60% in β-PFO for η= 0.30 V (*CD*= 7.5×10^{16} cm^{-3}; Fig. 4D).

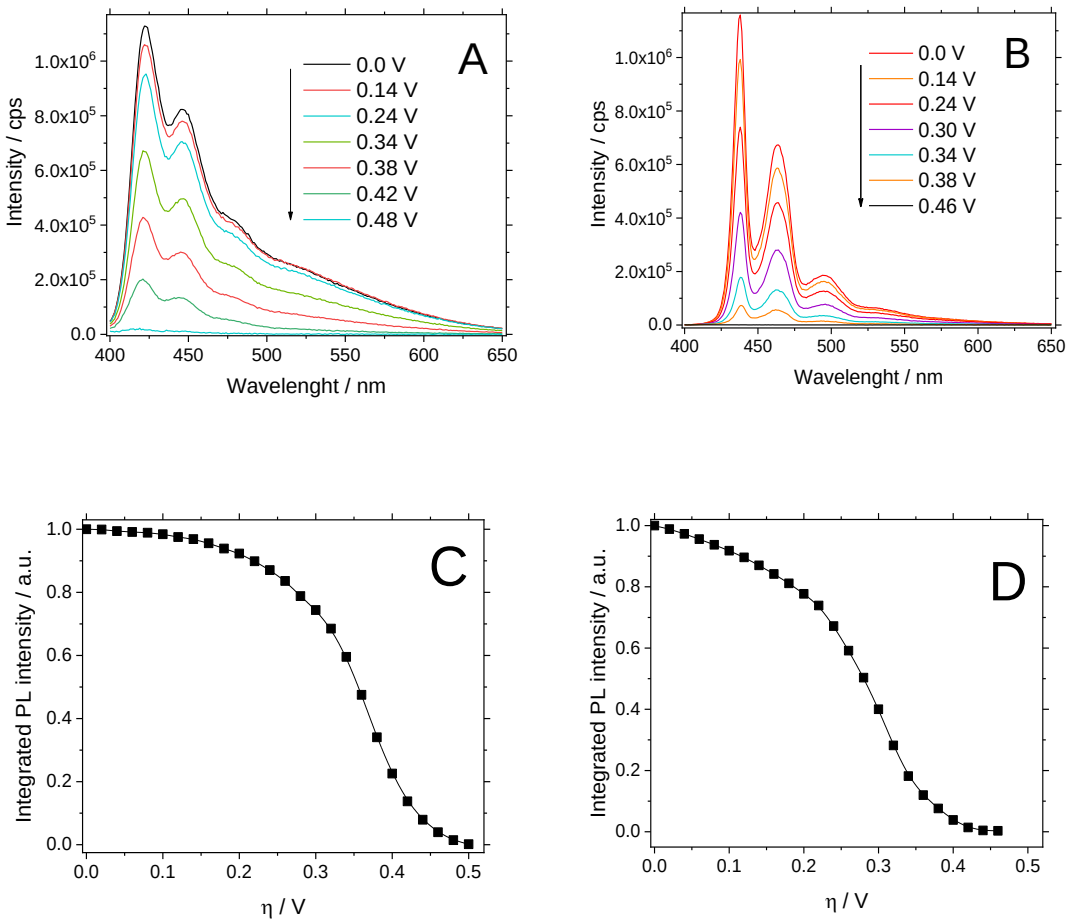

Figure 4. Evolution of the PL emission spectrum (λ_{exc}=380 nm) upon *p*-doping for **A)** α-PFO and **B)** β-PFO films. The integrated intensity of the PL emission against bias potential for **C)** α-PFO and **D)** β-PFO films.

In α-PFO films, electrochemical *p*-doping gives rise to a progressive quenching of fluorescence whose intensity (Fig. 4C) follows an almost perfect sigmoidal decay with the increasing bias potential. This behavior reveals that the quenching moieties are homogeneously distributed in the glassy polymer film, as modeled previously by van Reenen *et al.* [40]. On the contrary, the loss in β-PFO PL intensity exhibits two different trends roughly above and below η=0.2 V, i.e. at a polarization potential close to the

crossover point of CD vs. η curves in Fig. 2. The presence of α and β phases in the film can be at the origin of this two-step quenching behavior.

3.3. Analysis of exciton dynamics

It is well established that the charge injected during the electrochemical doping of conjugated polymers causes the quenching of PL by the generation of non-radiative decay paths for excitons. These paths involve bimolecular exciton-polaron annihilation events that compete with the conventional monomolecular decay from a higher energy (S_1) to the ground state (S_0). Hence, the electrochemical quenching process is usually represented as:

$$S_1 + p^+ \xrightarrow{k_q} S_0 + p^+ + phonons \qquad (1)$$

where k_q is the bimolecular quenching rate constant for the exciton-polaron annihilation, which depends on the mutual exciton-polaron diffusion rate. The annihilation process, which is responsible for the changes in the PL emission intensity in the presence of polarons, can be modeled with an expression equivalent to the classical Stern-Volmer equation [29]:

$$\frac{I_0}{I} = 1 + k_q \tau_0 [CD] \qquad (2)$$

where I_0 stands for the fluorescence intensity in the undoped state, I represents the attenuated emission intensity in the presence of quenchers and τ_0 is the exciton lifetime of the chromophore.

Stern-Volmer plots obtained from photoelectrochemical luminescence emission spectra of glassy and semicrystalline PFO samples are presented in Fig. 5. In both cases, two well-defined regions can be observed. On the one hand, almost linear trends are

distinguished at low doping levels, which can be ascribed to a diffusion-controlled process in dynamic quenching.

In situ UV reveals that the quenching at these doping levels is produced for a concentration of polarons below the detection limit of the experimental device. The process is dominated by dynamic quenching characterized by a time-independent bimolecular rate [43]. At higher doping level (for which the polaron band can be distinguished in the UV spectrum) the quenching mechanism can be better explained in terms of a static quenching contribution. Under these new conditions, polaronic bands hinder the formation of excited-state species.

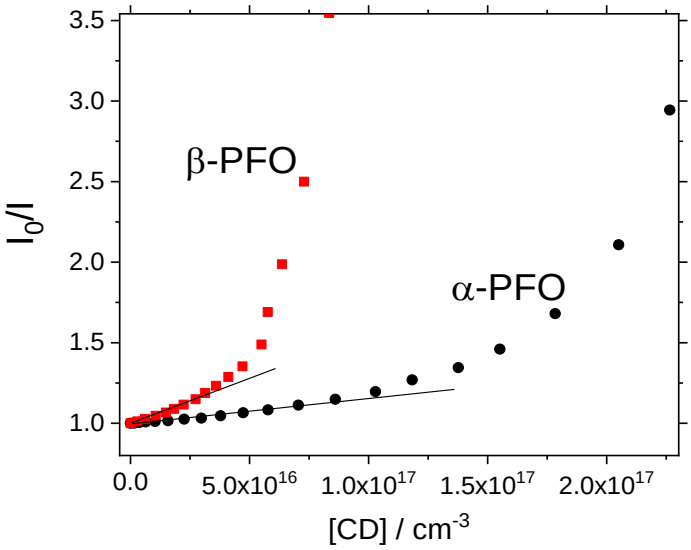

Figure 5. Electrochemical Stern-Volmer plots for the *p*-doping process at glassy (●) and semicrystalline PFO sample films (■).

On the other hand, positive deviations from the straight line occur at higher doping levels. Such a feature reveals that a sufficient concentration of electrochemically-generated polarons induces additional annihilation mechanisms, such as exciton-polaron energy transfer [43], which promote the complete quenching of the PL signal.

The electrochemical quenching usually provides time-independent quenching rates, which are diffusion-assisted for charge densities below 10^{17} cm^{-3}. Above those doping levels, mixed doping mechanisms including direct FRET, which dominates at high charge densities, can be found.

For α-PFO, the linear region of the Stern-Volmer plot extends up to doping levels beyond 7×10^{16} cm^{-3}. Such a value is three times higher than that of the semicrystalline material, suggesting that the dynamic quenching is favored in glassy domains over β-segments. This behavior is a consequence of an apparently faster diffusion of excitons in the ordered phases.

At this point, it is worth remembering (see discussion in Fig. 4) that the charge injected into the semicrystalline film is not homogeneously distributed, but rather confined within β-segments. Taking this effect into account and recalling that the fraction of ordered segments in β-PFO amounts to nearly 1/3, the actual charge density in the β-phase should triple the nominal charge density. Accordingly, the electrochemical Stern-Volmer plot was corrected by charge confinement and depicted in Fig. 6 for PFO samples.

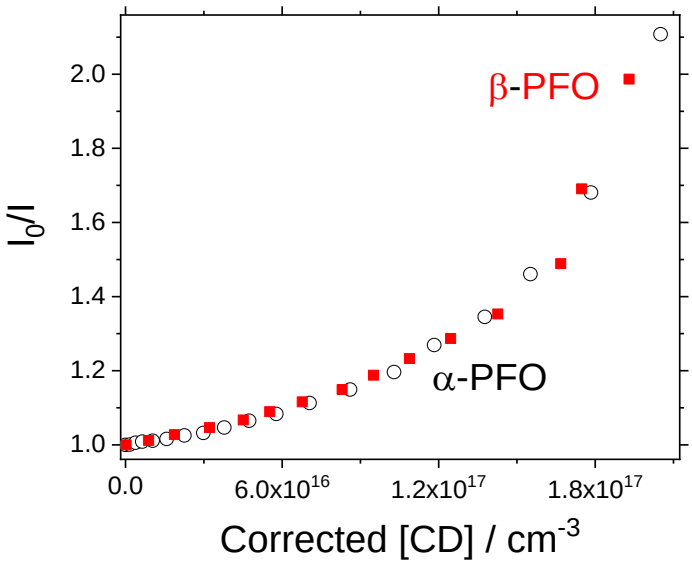

Figure 6. Stern-Volmer plots for glassy (○) and semicrystalline (■) PFO films after correction for the effect of charge confinement in the β-phase

The good agreement between responses for α- and β-PFO films strongly suggests that exciton diffusion coefficients are similar in both polymeric conformations, regardless of the concentration of β phase. Studies performed by Samuel et al.[26] have shown that exciton diffusion coefficients in PFO films containing β-phase present similar values to those of the glassy phase, despite excitons occupy a more reduced volume that may drive to faster exciton-exciton annihilation.

A better understanding of the exciton-polaron interaction processes in glassy and semicrystalline PFO materials can be reached by a suitable analysis of their PL emission spectra. The effect of applied potential on the spectral shape was analyzed by performing a gaussian deconvolution of the various electron-phonon coupling transitions in the fluorescence emission spectra (see Fig. S2 in the supporting information). Neither the shape of the α-PFO PL spectrum nor the position of its emission maximum seems to be significantly affected for charge densities below 6 $\times 10^{16}$ cm^{-3} ($\eta < 0.2$ V, Fig. S3). However, deeper polarization produces a 4-nm hypsochromic shift of the emission peak. Similar behavior was already described for other polymers such as MEH-PPV, for which a high density of quenchers seemed to reduce the probability of de-excitation at low energy sites and, consequently, the PL emission appeared blue-shifted [29]. The main signal of doped α-PFO suffers a hypsochromic shift as a result of emission from more energetic chromophores. The emission spectrum of the semicrystalline sample containing β-phase shows negligible changes at low to moderate bias potential. However, deconvoluted PL spectra display a very slight red-shift of the 0-0 vibronic transition above

η= 0.25 V. Only the 0-1 vibronic transition shifts clearly to the blue at η~ 0.35 V (Fig. S4).

The average coherence length of excitons in conjugated polymers can be estimated from the experimental, dimensionless parameter S_R [44,45]:

$$S_R = \frac{I_{00}}{I_{01}} \qquad (4)$$

where I_{00} and I_{01} are the 0-0 (zero-phonon) and 0-1 (first vibronic) intensities in the emission spectrum, respectively. The effect caused by the injected charge on the experimental values of S_R for PFO is displayed in Fig. 7. For the glassy α-PFO sample, S_R remains nearly constant at around 2.37 at a low doping level (*CD* below 6×10^{16} cm^{-3}) but sharply decreases to 1.95 beyond that limit. Such behavior reveals that the length of radiative excitons in a pure α-phase falls by 20% when a high concentration of polarons is injected. Regarding the semicrystalline PFO layer, excitons also remain unperturbed (constant S_R) up to a charge density of about 6×10^{16} cm^{-3}. However, the value for disperse excitons within this charge density interval amounts to about 1.7, revealing a significantly shorter exciton coherence length than that in the glassy material. The observed compression of the exciton size in β-phase enriched films could be ascribed to the stronger interactions between photogenerated charge pairs when planar, stacked polymer chains are present. At higher doping levels, an abrupt decrease in S_R is also observed, and hence further shortening of the exciton coherence length should be expected.

Since a three-dimensional homogeneous distribution of the injected charge inside the glassy polymer seems to be likely, the mean distance between generated polarons can be calculated from the Wigner-Seitz radius, r_{ws} [46,47]:

$$r_{ws} = \left(\frac{3}{4\pi[CD]}\right)^{1/3} \qquad (5)$$

Therefore, it can be deduced that polarons generated in glassy PFO at low doping levels (CD=6×10^{16} cm^{-3}) are separated by at least 23 nm. Since polarons are effective quenchers for excitons, this distance constitutes the upper limit for the exciton coherence length. On the other hand, the Wigner-Seitz radius calculated at high doping level (injected charge density above 15×10^{16} cm^{-3}) falls to 17 nm. This decrease agrees reasonably with that of S_R, which supports the close correspondence between the number of repeat units bearing a coherent exciton, N_c, and the average distance between injected polarons within the polymer film, irrespectively of their concentration.

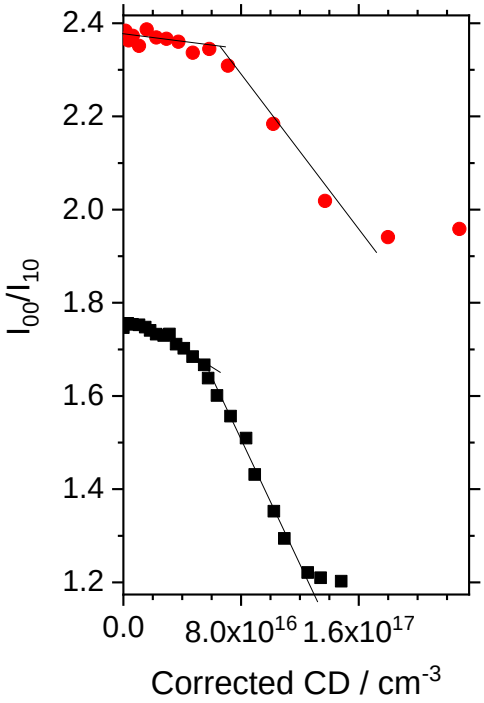

Figure 7. Experimental values of S_R at increasing doping level for glassy (●, red circles) and semicrystalline –β-phase containing– samples (■, black squares) of PFO. Spectroscopic data obtained from Fig. 5 and 6, respectively

S_R values are plotted in Fig. 8 against the Wigner-Seitz radius at different potentials within the region of the sudden S_R drop. Datasets for glassy and semicrystalline PFO films

fit well to the same straight line, thus confirming the existence of a close linear correlation between both parameters.

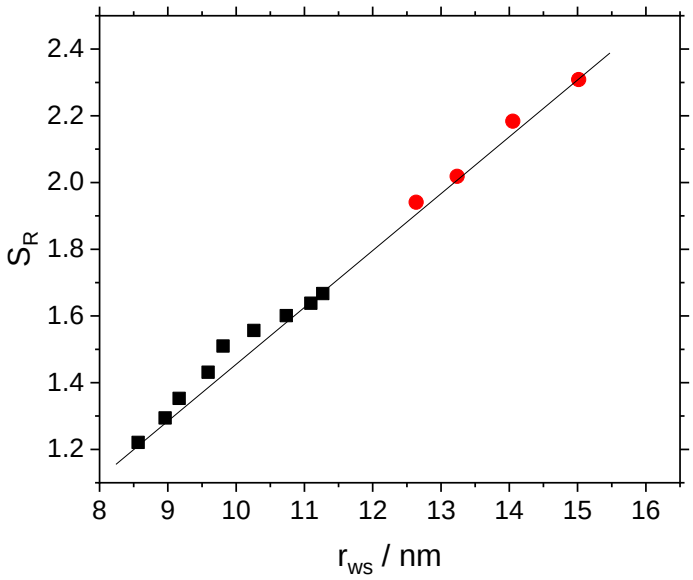

Figure 8. Linear correlation between S_R and Wigner-Seitz radius obtained for glassy (●, red circles) and semicrystalline (■, black squares) PFO films at different sample potentials.

From the slope of the linear regression, 0.15 nm^{-1}, the exciton coherence length for the polymer in the native state can be estimated. Spano *et al* [48,49] proposed an accurate relation between S_R and the number of repeat units over which the exciton is coherently delocalized, N_c:

$$S_R = \frac{k}{\lambda^2} N_c \qquad (6)$$

where λ^2 is the Huang-Rhys factor and k is a dimensionless parameter that is exactly unity in the Frenkel exciton limit for J-aggregates and deviates from unity for 1D semiconductors (i.e. conjugated polymers)[44,48] and N_c is the number of chromophores (repeat units) over which the exciton is coherently delocalized. The term $\frac{k}{\lambda^2}$ can be

considered as a constant S_R parameter for a single monomer in the chain and its value is unknown [50]. Eq. (6) can be rewritten in terms of the exciton coherence length, L_c:

$$S_R = \frac{k}{\lambda^2}\frac{L_c}{d} \qquad (7)$$

being d the repeat unit (monomer) size (d= 0.85 nm for PFO monomers[51]). Since the Wigner-Seitz radius is an upper limit for the exciton coherence length ($L_c \leq r_{ws}$), it must be satisfied that $\frac{S_R}{L_c} \geq 0.15$. This inequality allows an estimation of the upper limit for the coherence length of excitons from the S_R value of the pristine polymer films. For glassy PFO L_c≤16 nm, while a smaller value (12 nm) is obtained for excitons in the ordered β-phase.

4. Conclusions

Glassy and partially crystalline PFO samples were studied by a combination of electrochemical and spectroscopic methods. A close connection between the electrochemically measured HOMO level and the inner structure of PFO was found. At low doping levels, the injection of polarons is energetically less favored in glassy samples but the opposite is found at high doping levels. Optoelectronic alterations caused by *p*-doping process confirmed that charge injection occurs mainly in the more ordered β-phase.

In situ PL spectra recorded for α-PFO samples at increasing doping levels revealed that the quenching elements are homogeneously distributed throughout this material, resulting in a pure sigmoidal shape fluorescence quenching. On the contrary, a two-step process was observed for the semicrystalline material, which points to the presence of different phases containing either α or β structure. Stern-Volmer plots suggested that the dynamic quenching is favored in glassy domains over the ordered β-phase, probably

because of the faster diffusion of excitons in the ordered material. Indeed, the Stern-Volmer plots corrected by charge confinement in β segments showed good agreement between both quenching responses. The Wigner-Seitz radius and the dimensionless parameter S_R were correlated to estimate the exciton coherence lengths in glassy and crystalline domains (16 and 12 nm, respectively). Hence, a single exciton is distributed over about 20 monomer units in the α-PFO material but only over 14 units in β-PFO.

Acknowledgments

The authors would like to thank Spanish *Ministerio de Ciencia e Innovación* (projects PID2019-105923RB-I00, PDC2021-120884-I00, European Union NextGenerationEU PRTR-C17.I1) and *Generalitat Valenciana* (project GVA-THINKINAZUL/2021/015 and PROMETEO/2018/087) for financial support.

References

[1] S. Günes, H. Neugebauer, N. S. Sariciftci, *Chem. Rev.* **2007**, *107*, 1324.

[2] S. Allard, M. Forster, B. Souharce, H. Thiem, U. Scherf, *Angew. Chemie Int. Ed.* **2008**, *47*, 4070.

[3] P. C. Y. Chow, T. Someya, *Adv. Mater.* **2020**, *32*, 1902045.

[4] Q. Zhang, J. Liu, Q. Wei, X. Guo, Y. Xu, R. Xia, L. Xie, Y. Qian, C. Sun, L. Lüer, J. Cabanillas-Gonzalez, D. D. C. Bradley, W. Huang, *Adv. Funct. Mater.* **2018**, *28*, 1705824.

[5] G.-H. Lee, H. Moon, H. Kim, G. H. Lee, W. Kwon, S. Yoo, D. Myung, S. H. Yun, Z. Bao, S. K. Hahn, *Nat. Rev. Mater.* **2020**, *5*, 149.

[6] S. Schlisske, C. Rosenauer, T. Rödlmeier, K. Giringer, J. J. Michels, K. Kremer, U. Lemmer, S. Morsbach, K. C. Daoulas, G. Hernandez-Sosa, *Adv. Mater. Technol.* **2021**, *6*, 2000335.

[7] Y. Liu, J. Zhao, Z. Li, C. Mu, W. Ma, H. Hu, K. Jiang, H. Lin, H. Ade, H. Yan, *Nat. Commun.* **2014**, *5*, 5293.

[8] R. Coehoorn, L. Zhang, P. A. Bobbert, H. van Eersel, *Phys. Rev. B* **2017**, *95*, 134202.

[9] F. C. Spano, *Acc. Chem. Res.* **2010**, *43*, 429.

[10] G. D. Scholes, G. Rumbles, *Nat. Mater.* **2006**, *5*, 683.

[11] W. Barford, *J. Phys. Chem. A* **2013**, *117*, 2665.

[12] A. De Sio, F. Troiani, M. Maiuri, J. Réhault, E. Sommer, J. Lim, S. F. Huelga, M. B. Plenio, C. A. Rozzi, G. Cerullo, E. Molinari, C. Lienau, *Nat. Commun.* **2016**, *7*, 1.

[13] F. C. Spano, C. Silva, *Annu. Rev. Phys. Chem.* **2014**, *65*, 477.

[14] I. Hwang, G. D. Scholes, *Chem. Mater.* **2011**, *23*, 610.

[15] A. De Sio, F. Troiani, M. Maiuri, J. Réhault, E. Sommer, J. Lim, S. F. Huelga, M. B. Plenio, C. A. Rozzi, G. Cerullo, E. Molinari, C. Lienau, *Nat. Commun.* **2016**, *7*, 1.

[16] X. H. Jin, M. B. Price, J. R. Finnegan, C. E. Boott, J. M. Richter, A. Rao, S. Matthew Menke, R. H. Friend, G. R. Whittell, I. Manners, *Science (80-.).* **2018**, *360*, 897.

[17] M. Ni, X. An, L. Bai, K. Wang, J. Cai, S. Wang, L. He, M. Xu, H. Liu, J. Lin, X.

Ding, C. Yin, W. Huang, *Adv. Funct. Mater.* **2022**, *32*, 2106564.

[18] M. Ariu, D. G. Lidzey, M. Sims, A. J. Cadby, P. A. Lane, D. D. C. Bradley, *J. Physics-Condensed Matter* **2002**, *14*, 9975.

[19] L. Huang, T. Li, B. Liu, L. Zhang, Z. Bai, X. Li, X. Huang, D. Lu, *Soft Matter* **2015**, *11*, 2627.

[20] M. Knaapila, A. P. Monkman, *Adv. Mater.* **2013**, *25*, 1090.

[21] S. Fratini, M. Nikolka, A. Salleo, G. Schweicher, H. Sirringhaus, *Nat. Mater.* **2020**, *19*, 491.

[22] T. Kreouzis, D. Poplavskyy, S. M. Tuladhar, M. Campoy-Quiles, J. Nelson, A. J. Campbell, D. D. C. Bradley, *Phys. Rev. B* **2006**, *73*, 235201.

[23] M. Redecker, D. D. C. Bradley, M. Inbasekaran, E. P. Woo, *Appl. Phys. Lett.* **1998**, *73*, 1565.

[24] R. Noriega, J. Rivnay, K. Vandewal, F. P. V Koch, N. Stingelin, P. Smith, M. F. Toney, A. Salleo, *Nat. Mater.* **2013**, *12*, 1038.

[25] A. J. Cadby, P. A. Lane, H. Mellor, S. J. Martin, M. Grell, C. Giebeler, D. D. C. Bradley, M. Wohlgenannt, C. An, Z. V. Vardeny, *Phys. Rev. B* **2000**, *62*, 15604.

[26] P. E. Shaw, A. Ruseckas, J. Peet, G. C. Bazan, I. D. W. Samuel, *Adv. Funct. Mater.* **2010**, *20*, 155.

[27] M. N. Yu, H. Soleimaninejad, J. Y. Lin, Z. Y. Zuo, B. Liu, Y. F. Bo, L. B. Bai, Y. M. Han, T. A. Smith, M. Xu, X. P. Wu, D. E. Dunstan, R. D. Xia, L. H. Xie, D. D. C. Bradley, W. Huang, *J. Phys. Chem. Lett.* **2018**, *9*, 364.

[28] G. Redmond, *Chem. Mater.* **2008**, *20*, 6501.

[29] F. Montilla, A. F. Quintero-Jaime, F. Huerta, C. Quijada, *Electrochim. Acta* **2021**, *387*, 138419.

[30] F. Montilla, R. Mallavia, *Adv. Funct. Mater.* **2007**, *17*, 71.

[31] M. Fakis, I. Polyzos, G. Tsigaridas, V. Giannetas, P. Persephonis, *Chem. Phys. Lett.* **2004**, *394*, 372.

[32] F. Montilla, F. Huerta, in *Lumin. Electrochem.* (Eds.: P. Audebert, F. Miomandre), Springer International Publishing, Cham, **2017**, pp. 105–137.

[33] J. Wollmann, F.-J. Kahle, I. Bauer, A. Köhler, P. Strohriegl, *Macromolecules* **2020**, *53*, 10137.

[34] F. Montilla, A. Ruseckas, I. D. W. W. Samuel, *Chem. Phys. Lett.* **2013**, *585*, 133.

[35] A. K. Bansal, A. Ruseckas, P. E. Shaw, I. D. W. Samuel, *J. Phys. Chem. C* **2010**, *114*, 17864.

[36] S. Trasatti, *Pure Appl. Chem.* **1986**, *58*, 955.

[37] B. Liu, W.-L. Yu, Y.-H. Lai, W. Huang, *Chem. Mater.* **2001**, *13*, 1984.

[38] S. Kilina, E. R. Batista, P. Yang, S. Tretiak, A. Saxena, R. L. Martin, D. L. Smith, *ACS Nano* **2008**, *2*, 1381.

[39] J. Gierschner, J. Cornil, H. J. Egelhaaf, *Adv. Mater.* **2007**, *19*, 173.

[40] S. van Reenen, M. V Vitorino, S. C. J. Meskers, R. A. J. Janssen, M. Kemerink, *Phys. Rev. B* **2014**, *89*.

[41] E. Kaya, A. Balan, D. Baran, A. Cirpan, L. Toppare, *Org. Electron.* **2011**, *12*, 202.

[42] M. Ariu, M. Sims, M. D. Rahn, J. Hill, A. M. Fox, D. G. Lidzey, M. Oda, J.

Cabanillas-Gonzalez, D. D. C. Bradley, *Phys. Rev. B* **2003**, *67*, 195333.

[43] F. Montilla, A. Ruseckas, I. D. W. Samuel, *J. Phys. Chem. C* **2018**, *122*, 9766.

[44] G. D. Scholes, *Faraday Discuss.* **2019**, *221*, 265.

[45] H. J. Eggimann, F. Le Roux, L. M. Herz, *J. Phys. Chem. Lett.* **2019**, *10*, 1729.

[46] J. Stejskal, M. Trchová, Z. Morávková, P. Bober, M. Bláha, J. Pfleger, P. Magdziarz, J. Prokeš, M. Havlicek, N. S. Sariciftci, A. Sperlich, V. Dyakonov, Z. Zujovic, *J. Solid State Electrochem.* **2015**, *19*, 2653.

[47] B. Yurash, H. Nakanotani, Y. Olivier, D. Beljonne, C. Adachi, T. Q. Nguyen, *Adv. Mater.* **2019**, *31*, 1804490.

[48] H. Yamagata, F. C. Spano, *J. Phys. Chem. Lett.* **2014**, *5*, 622.

[49] F. C. Spano, H. Yamagata, *J. Phys. Chem. B* **2010**, *115*, 5133.

[50] T. W. Tseng, H. Yan, T. Nakamura, S. Omagari, J. S. Kim, M. Vacha, *ACS Nano* **2020**, *14*, 16096.

[51] S. H. Chen, H. L. Chou, A. C. Su, S. A. Chen, *Macromolecules* **2004**, *37*, 6833.